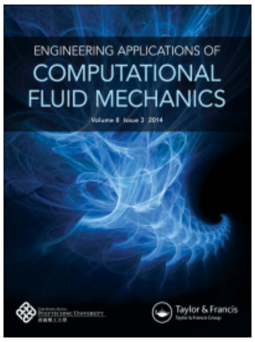

Engineering Applications of Computational Fluid Mechanics

ISSN: (Print) (Online) Journal homepage: www.tandfonline.com/journals/tcfm20

Correlation between cargo properties and train overturning safety for a high-speed freight train under strong winds

Duo Zhang, Zhan-Hao Guo, Yi-Qing Ni, Zheng-Wei Chen, Wai Kei Ao, Amir Bordbar & Fang-Ru Zhou

To cite this article: Duo Zhang, Zhan-Hao Guo, Yi-Qing Ni, Zheng-Wei Chen, Wai Kei Ao, Amir Bordbar & Fang-Ru Zhou (2023) Correlation between cargo properties and train overturning safety for a high-speed freight train under strong winds, Engineering Applications of Computational Fluid Mechanics, 17:1, 2221308, DOI: 10.1080/19942060.2023.2221308

To link to this article: https://doi.org/10.1080/19942060.2023.2221308

ENGINEERING APPLICATIONS OF COMPUTATIONAL FLUID MECHANICS
2023, VOL. 17, NO. 1, 2221308
https://doi.org/10.1080/19942060.2023.2221308

Taylor & Francis
Taylor & Francis Group

Correlation between cargo properties and train overturning safety for a high-speed freight train under strong winds

Duo Zhang[a,b], Zhan-Hao Guo[a,b], Yi-Qing Ni[a,b], Zheng-Wei Chen[a,b], Wai Kei Ao[a,b], Amir Bordbar[c] and Fang-Ru Zhou[d,e]

[a]National Rail Transit Electrification and Automation Engineering Technology Research Center (Hong Kong Branch), Hong Kong, People's Republic of China; [b]Department of Civil and Environmental Engineering, The Hong Kong Polytechnic University, Hong Kong, People's Republic of China; [c]School of Engineering, Computing and Mathematics, University of Plymouth, Plymouth, UK; [d]School of Transportation & Logistics, Southwest Jiaotong University, Chengdu, People's Republic of China; [e]National United Engineering Laboratory of Integrated and Intelligent Transportation, Southwest Jiaotong University, Chengdu, People's Republic of China

ABSTRACT

The high-speed railway has become an important passenger transport mode. Relying on the abundant passenger transport experience and expansive railway network, the high-speed freight train (HSFT) is feasible to be developed and has great application potential. As a critical component of HSFT, the cargo plays an important role in the overturning safety of HSFT under strong wind conditions. Previous studies about the aerodynamic performance of the high-speed train usually regarded the loaded carbody as an individual rigid body. Limited attention was paid to the variability inside the vehicle. In order to improve the running safety of HSFT under strong wind conditions, the multibody dynamics simulation is adopted to demonstrate the effect of cargo property on the overturning risk of HSFT under the aerodynamic loads obtained through the computational fluid dynamics (CFD) simulations. It is demonstrated that the inner side crosswind is more dangerous than the outer side crosswind. The speed of HSFT should be limited according to the cargo quantity, and the maximum speed for a fully loaded HSFT can be 305 km/h when the crosswind velocity is 20 m/s. The larger cargo density should be encouraged because it is good for train overturning safety in severe working conditions.

ARTICLE HISTORY
Received 20 February 2023
Accepted 26 May 2023

KEYWORDS
High-speed freight train; Cargo properties; Overturning safety; Crosswinds; Computational fluid dynamics; Multibody dynamics

1. Introduction

The high-speed train has become a superior means of passenger transportation all over the world. Considering its remarkable performance in running safety, transport efficiency, and low-carbon energy generation, the high-speed train can also be the potential solution to modern freight transportation, especially for low-density high value (LDHV) goods (Boehm et al., 2021; Zhang et al., 2023). Shifting freight traffic from roads and air to the high-speed railway has attracted attention because of the increased concern about incremental fuel prices, congestion, and environmental pollution (Watson et al., 2018; Watson et al., 2019). In Germany, a logistics concept based on the specially designed freight train, NGT CARGO, was proposed and is being developed by DLR (Schubert et al., 2014). China Railway has better progress. The prototype of Chinese HSFT, which is designed based on the current high-speed passenger train, was off the assembly line at the end of 2020 (China Youth International, 2020). The LDHV goods and fluid cargo are planned to be transported using containers loaded on HSFT. Thus, it is pressing to formulate the technical specifications of HSFT for its safe operation in the future (Figure 1).

The running safety of high-speed train is seriously affected by crosswind (Deng et al., 2020). Although the operation requirements on the high-speed passenger train have been well developed, they are not enough for HSFT because there are significant differences between these two kinds of trains. For HSFT, the cargo mass can be quite large and fluctuate sharply so as to have an significant effect on the response of the train in a strong wind area (Liu et al., 2018). Thus, it is very necessary to investigate the requisite cargo properties for HSFT under strong wind conditions.

As an innovative transportation mode, the study on the HSFT is just getting started. The mounting system between containers and the vehicle was proven to play an important role in the vertical vibration of vehicle-container coupled system (Xue et al., 2022). Considering

CONTACT Zheng-Wei Chen zhengwei.chen@polyu.edu.hk Z105, 1/F, Block Z, The Hong Kong Polytechnic University, Hung Hom, Kowloon, Hong Kong

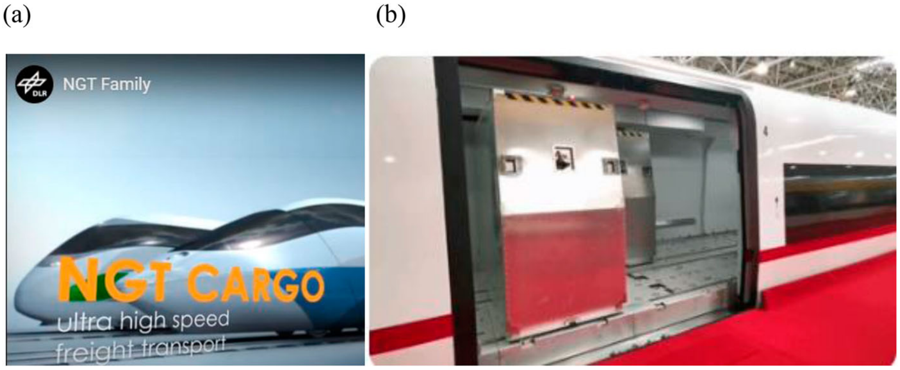

Figure 1. Innovative high-speed freight trains: (a) conceptual graph of NGT CARGO (German Aerospace Center, 2018); and (b) photo of Chinese HSFT (Optoelectronics Science And Technology, 2020).

the unique characteristic of transporting both solid and fluid goods, it was demonstrated that overturning safety for HSFT could be significantly affected by liquid sloshing (Deng et al., 2021). However, regrettably, the former studies didn't take into account the effect of strong wind which is a key threat to the running safety of HSFT.

Before the appearance of HSFT, the traditional high-speed freight vehicle was designed through improvements in the running gear of wagons (Iwnicki et al., 2013) and could run as fast as 160 km/h (Watson et al., 2018). When studying the aerodynamic performance of the traditional high-speed freight train, freight trains with special geometry were primarily focused on, such as the double-stacked wagon and container wagon (Maleki et al., 2020; Soper, 2016). As can be seen, although the effect of crosswind on the traditional high-speed freight vehicle was considered, the role of cargo properties was not studied.

Because the HSFT will be used for transporting LDHV goods and fluid cargo, the goods inside the carbody can be deemed distributed symmetrically. Thus, more cargo will result in larger cargo mass and higher gravity center in the meantime. For a conventional freight wagon, the height of gravity center obviously has a significant influence on the running safety (Yang et al., 2021; Zhang et al., 2021, 2022). Similarly, decreasing the height of gravity center has been widely recognized as a beneficial solution for the high-speed passenger train in case there are strong winds (Thomas et al., 2010). On the other hand, increasing the vehicle mass is necessary for guaranteeing the overturning safety of a high-speed passenger train (Heleno et al., 2021). Hence, the increase in cargo quantity may play a positive role in vehicle running safety because the vehicle mass rises, but may conversely play a negative role because the gravity center height is also affected. It is necessary to clarify the relationship between the running safety and cargo quantity for a high-speed train under strong wind conditions. Because the research objective is cargo quantity, which can determine the height of gravity center and vehicle mass simultaneously, the loaded carbody should not be modelled as an individual body as the former studies did. The cargo will be variable and connected with the carbody by a fixed joint to highlight the characteristics of HSFT. The cargo density could be an important parameter in this model. Moreover, due to the action of centrifugal force on the curve track, the vehicle speed, wind direction, and curve radius have significant effects on the dynamic performance of HSFT. Thus, different simulation cases will be considered in this paper.

The overturning coefficient can be adopted as the criterion for evaluating vehicle running safety under strong wind conditions (Chen et al., 2022; EN, 2010). The computational fluid dynamics method can be used to obtain the aerodynamic loads of HSFT (Chen et al., 2020).

In the second part of this work, a crosswind-vehicle vibration model is developed to reveal the correlation between the overturning coefficient and representative vehicle and cargo parameters, such as cargo quantity, cargo density, and vehicle speed. In Section 3, the aerodynamic loads for HSFT are obtained based on the computational fluid dynamics results and get validated by the wind tunnel test. In Section 4, the multibody dynamics model of HSFT is established and verified by the in-situ test data. The dynamic response of HSFT negotiating the curve track with the maximum aerodynamic load is simulated and investigated.

2. Vibration model of the vehicle with crosswinds

Due to the super elevation and centrifugal force, the vehicle running safety will get worse when HSFT goes through the curve track. Furthermore, under strong wind, the carbody vibration will be amplified to induce the risk of overturning. In order to reveal the influencing

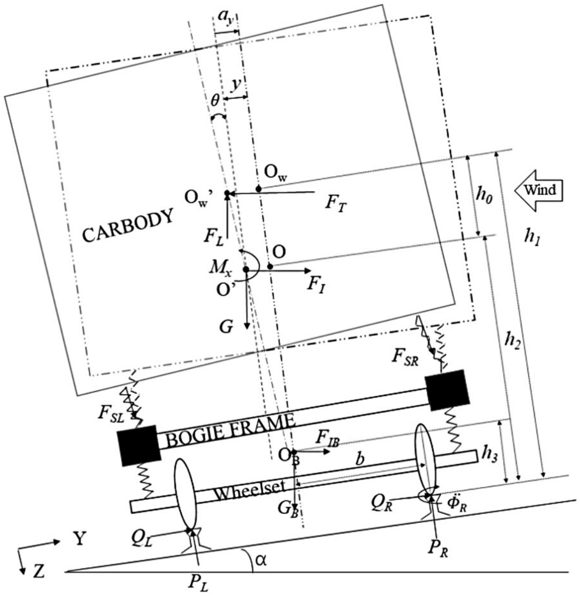

Figure 2. Front elevation of the vehicle model, where O and O′ denote the initial and current car body gravity centers respectively, O_W and $O_W{}'$ denote the initial and current wind force centers respectively, O_B denotes the bogie gravity center.

factors of the train overturning safety, the lateral vibration model of the vehicle when it is on a left-curved track is illustrated in Figure 2.

As an example, the crosswind is from the right-hand side and the vibration of the carbody is toward the right direction. The lateral movement of bogie can be ignored in the model because it is slight compared with the car body (Hibino et al., 2010).

The overturning coefficient is defined as:

$$D = \frac{P_L - P_R}{P_L + P_R} \tag{1}$$

where $P_L$and P_R are the vertical wheel-rail force on the left track and right track respectively.

In order to figure out the expression of overturning coefficient, all the forces and movements shown in Figure 2 are analyzed in the coordinate system of rail track.

When the whole vehicle is regarded as the calculation objective, the internal force is not considered. Because it is proved that the rolling and lateral movement of the car body are significantly greater than the vertical movement induced by the rolling motion (Liu et al., 2020), the sum of vertical wheel-rail forces can be calculated as:

$$P_L + P_R = G_Z + F_{IZ} + G_{BZ} + F_{IBZ} - F_{LZ} - F_{TZ} \tag{2}$$

where G is the gravity force of car body, F_I is the centrifugal force of car body, G_B is the gravity force of bogie, $F_{IB}$is the centrifugal force of bogie, F_L is the lift wind force, $F_T$is the side wind force, the subscript Z denotes the component force of these forces in the vertical direction of the track.

As illustrated in Figure 2, the rolling of the car body around its gravity center, which is represented by O, will result in the rolling acceleration of the vehicle's gravity center around the wheel-rail contact point on the right track. The vertical displacement of the wind force center can be neglected because its value is tiny. Hence, the rolling equation of the vehicle can be expressed as:

$$\begin{aligned} &P_L \cdot 2b + (F_{LZ} + F_{TZ}) \cdot (b + y + \theta h_0) + (F_{LY} - F_{TY}) \\ &\quad \cdot h_1 - (G_Z + F_{IZ}) \cdot (b + y) + (F_{IY} - G_Y) \\ &\quad \cdot h_2 - (G_{BZ} + F_{IBZ}) \cdot b \\ &\quad + (F_{IBY} - G_{BY}) \cdot h_3 - \gamma M_x = I_{xx}\ddot{\phi}_R \end{aligned} \tag{3}$$

where subscript Y denotes the component force of these forces in the lateral direction of the track, b is half of the distance between the wheel-rail contact points, y is the lateral displacement of the car body, θ is the rolling angle of the car body around its gravity center, h_1, h_2 and h_3 are the heights of the wind force center, car body gravity center and bogie gravity center from the rail top respectively, h_0 is the height of the wind force center from the car body gravity center, M_x is the rolling moment induced by wind force and is expanded by γ when calculating the moment around the wheel-rail contact point, I_{xx} and $\ddot{\phi}_R$ are the inertia moment and rolling acceleration around the contact point.

Under strong wind conditions, the vibration frequency of the car body is below 1 Hz (Wang, 1994). Thus, the damping force is not considered in this model. Then the lateral motion equation of the car body is:

$$F_{IY} - G_Y + F_{LY} - F_{TY} + F_{SLY} + F_{SRY} = M_L a_y \tag{4}$$

where F_{SL} and F_{SR} are the secondary suspension forces on the left side and right side respectively, M_L is the mass of loaded car body, a_y is the lateral acceleration of car body.

By combining Equations (2) and (3), the following is obtained:

$$D = \frac{y}{b} + \frac{\begin{array}{c} I_{xx}\ddot{\phi}_R - \gamma M_x - (G_{BZ} + F_{IBZ}) \cdot y \\ -(F_{LZ} + F_{TZ}) \cdot \theta h_0 - (F_{LY} - F_{TY}) \cdot h_1 \\ -(F_{IY} - G_Y) \cdot h_2 - (F_{IBY} - G_{BY}) \cdot h_3 \end{array}}{b \cdot (G_Z + F_{IZ} + G_{BZ} + F_{IBZ} - F_{LZ} - F_{TZ})} \tag{5}$$

It is obvious that

$$h_0 = h_1 - h_2 \tag{6}$$

Equation (5) can be expressed as:

$$D=\frac{y}{b}+\frac{\begin{array}{c}I_{xx}\ddot{\phi}_R-\gamma M_x-(G_{BZ}+F_{IBZ})\cdot y\\+[(F_{IY}-G_Y)-(F_{LZ}+F_{TZ})\cdot\theta]\cdot h_0\\-(F_{LY}-F_{TY}+F_{IY}-G_Y)\cdot h_1\\-(F_{IBY}-G_{BY})\cdot h_3\end{array}}{b\cdot(G_Z+F_{IZ}+G_{BZ}+F_{IBZ}-F_{LZ}-F_{TZ})} \tag{7}$$

If the lateral stiffness of the secondary suspension for each side is defined as K, it can be obtained that:

$$F_{SLY}+F_{SRY}=2Ky \tag{8}$$

By substituting Equations (4) and (8) into Equation (7):

$$D=\frac{y}{b}+\frac{\begin{array}{c}I_{xx}\ddot{\phi}_R-\gamma M_x-(G_{BZ}+F_{IBZ})\cdot y\\-[(F_{IY}-G_Y)-(F_{LZ}+F_{TZ})\cdot\theta]\cdot h_0\\-(M_La_y-2Ky)\cdot h_1-(F_{IBY}-G_{BY})\\\cdot h_3\end{array}}{b\cdot(G_Z+F_{IZ}+G_{BZ}+F_{IBZ}-F_{LZ}-F_{TZ})} \tag{9}$$

Because θ is usually smaller than 0.05 rad (Liu et al., 2022), Equation (9) can be simplified as:

$$D=\frac{y}{b}+\frac{\begin{array}{c}I_{xx}\ddot{\phi}_R-\gamma M_x-(G_{BZ}+F_{IBZ})\cdot y\\-(F_{IY}-G_Y)\cdot h_0-(M_La_y-2Ky)\\\cdot h_1-(F_{IBY}-G_{BY})\cdot h_3\end{array}}{b\cdot(G_Z+F_{IZ}+G_{BZ}+F_{IBZ}-F_{LZ}-F_{TZ})} \tag{10}$$

According to Figure 2, it is easy to calculate the component forces of each gravity force and centrifugal force, as well as the lift and side wind force:

$$A=G_{BZ}+F_{IBZ}=M_Bg\cos\alpha+M_B\frac{v^2}{R}\sin\alpha \tag{11}$$

$$B=F_{IY}-G_Y=M_L\frac{v^2}{R}\cos\alpha-M_Lg\sin\alpha \tag{12}$$

$$C=F_{IBY}-G_{BY}=M_B\frac{v^2}{R}\cos\alpha-M_Bg\sin\alpha \tag{13}$$

$$\begin{aligned}E&=G_Z+F_{IZ}+G_{BZ}+F_{IBZ}-F_{LZ}-F_{TZ}\\&=M_Lg\cos\alpha+M_L\frac{v^2}{R}\sin\alpha+M_Bg\cos\alpha\\&\quad+M_B\frac{v^2}{R}\sin\alpha-F_L\cos\alpha-F_T\sin\alpha\end{aligned} \tag{14}$$

where M_B is the mass of bogie, v is the train velocity, R is the radius of curve track, α is the cant angle.

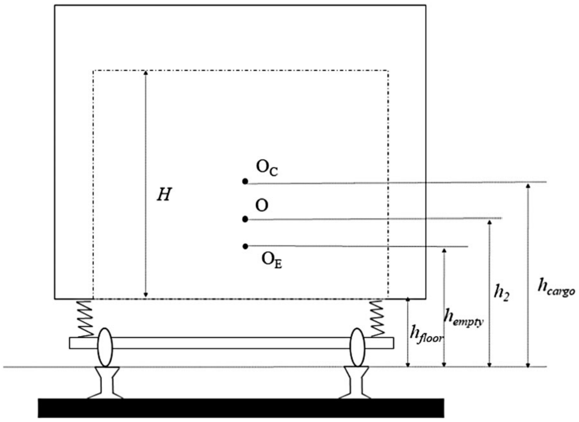

Figure 3. The height of a loaded car body.

By substituting Equations (6) and (11)–(14) into Equation (10), a complex calculation expression of overturning coefficient can be obtained as:

$$D=\frac{y}{b}+\frac{\begin{array}{c}I_{xx}\ddot{\phi}_R-\gamma M_x-Ay-(B+M_La_y\\-2Ky)\cdot h_1+Bh_2-Ch_3\end{array}}{Eb} \tag{15}$$

For a high-speed freight train, the values of M_B, b, h_1 and h_3 are constant, and the cargo properties determine the values of M_L and h_2. Because the cargo transported by the vehicle is liquid or in small pieces, a symmetrical cube is adopted to represent the cargo in Figure 3.

where O_C is the cargo gravity center, O_E is the gravity center of the empty car body, H is the height of the cargo, h_{cargo}, h_{empty} and h_{floor} are the heights to O_C, O_E, and car floor from the top of rail respectively.

The mass of cargo in a unit height can be assumed as η. If the mass of the empty car body is represented by M_E, values of M_L and h_2 can be calculated as:

$$M_L=M_E+\eta H \tag{16}$$

$$h_2=\frac{M_E\cdot h_{empty}+\eta H(0.5H+h_{floor})}{M_E+\eta H} \tag{17}$$

Based on Equations (15)–(17), it can be found that the cant deficiency, which is reflected in B and C, has a significant effect on the overturning coefficient. The lift and side wind force should also be focused on. Furthermore, cargo quantity and density play critical roles in train overturning safety.

3. Aerodynamics simulation of the crosswind-vehicle model

HSFT is designed based on the current high-speed passenger train by adjusting the usage mode of inner space. In this work, the Chinese eight-car CRH2C high-speed train is regarded as the substitution of HSFT. The curve radius of track is 7000 m and the super elevation is 150 mm (National Railway Administration of People's Republic of China, 2014). The maximum design speed of CRH2C is 350 km/h. Based on the analysis in Section 2, the cant deficiency has a significant effect on overturning coefficient. In order to cover a wide range of cant deficiency, the running speeds of the CRH2C model are designed as 69.83, 77.61, 84.68, 91.20, and 97.20 m/s respectively, while the wind velocity is 20 m/s in all cases.

3.1. Computational models

The CRH2C model is shown in Figure 4. Its total length, width and height are 201, 3.38 and 3.70 m, respectively. As shown in Figure 5, underneath the train, a simplified single track ballast bed was adopted, which is 0.02 m (the height of the track) away from the train. Figure 6 presents the relative positions of the train in computational domain. To avoid the boundary serious effect of flow fields around the train, the windward inlet (surface ABEF) is 60 m from the train, the head inlet (surface ABCD) is 80 m, the leeward outlet (surface CDHG) is 100 m, and the tail outlet (surface EFHG) is 200 m. In the simulation, the windward and head inlets were treated as the uniform velocity inlet boundary conditions, while the leeward and tail outlets being treated as the zero-pressure outlet boundary conditions. The train, ballast bed and ground were assigned as no-slip wall boundary conditions, while the symmetry boundary condition was used on the top of the computational domain (surface ACEH).

As mentioned above, there are five possible velocities for the train, while the velocity of the wind keeps constant. In order to reveal the interaction between the train and wind, a relative velocity was applied to the velocity inlet boundary conditions. As shown in Figure 7, relative velocity V_α is equal to $\sqrt{V_w^2 + V_{tr}^2}$, where V_w and V_{tr} represent the wind velocity and train velocity, respectively. In addition, the relative wind angle β can be calculated by $\tan\beta = V_w \sin\beta_w/(V_{tr} + V_w \cos\beta_w)$, where β_w refers to the actual wind angle, which is equal to 90°. According to the formulation above, Table 1 lists corresponding parameters in each case.

Figure 4. Train model and its parameters (Unit: m).

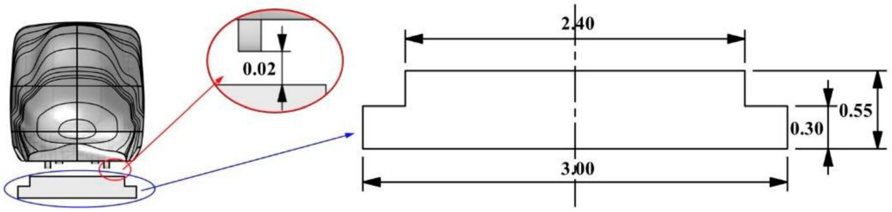

Figure 5. Ballast bed and its parameters (Unit: m).

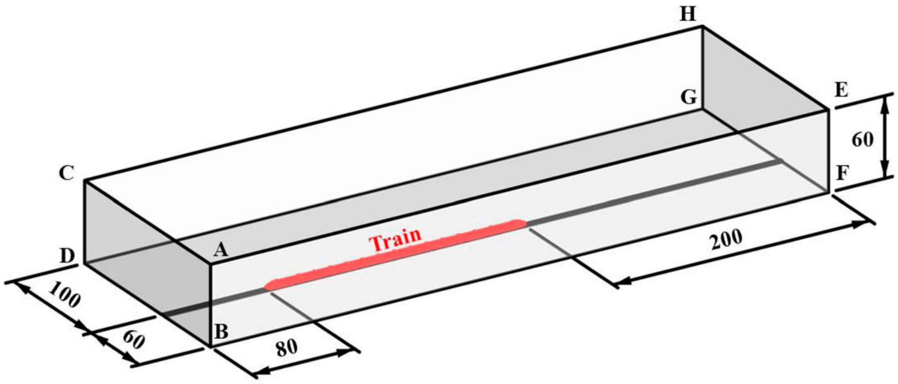

Figure 6. Computational domain and its parameters (Unit: m).

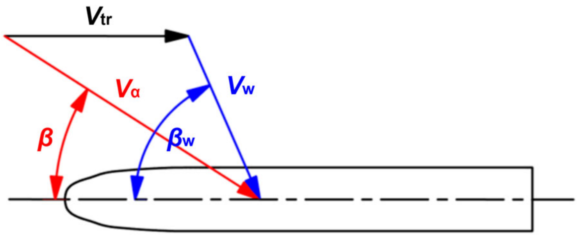

Figure 7. Relative velocity between the train and wind.

Table 1. The aerodynamic simulation parameters in each case.

	V_{tr} (m/s)	V_W (m/s)	V_α (m/s)	β_W (°)	β (°)
Case1	69.83	20.00	72.64	90	15.98
Case2	77.61	20.00	80.15	90	14.45
Case3	84.68	20.00	87.01	90	13.29
Case4	91.20	20.00	93.37	90	12.37
Case5	97.20	20.00	99.24	90	11.63

3.2. Computational mesh and numerical methods

A Poly-Hexacore mesh in Fluent meshing was adopted in all simulations of this Section. The surface meshes on the head car are shown in Figure 8, while the volume meshes around the head car are illustrated in Figure 9. To predict the turbulent boundary layer, ten prism layers are constructed on the surface of the train. In addition, because the vortices in the wake region and leeward side region are the main factors affecting the aerodynamics of the train, the meshes in these regions are refined to capture the corresponding vortices as much as possible. The total number of elements is approximately 30 million.

All the simulations in this study were performed in FLUENT 2020R2, a commercial computational fluid dynamics software. An unsteady, uncompressible solver was used, which is based on the shear stress transport (SST) k-ω turbulence model. The Semi-Implicit Method for Pressure-Linked Equations (SIMPLE) algorithm was chosen for coupling the pressure and velocity field. The Least Squares Cell Based algorithm was applied to compute gradient terms in all equations. To ensure computational accuracy, second-order accuracy discretization schemes were employed in all equations. To realize the time advance process, the second-order implicit scheme was used in time terms, and the time step was set as 1×10^{-4} s.

To verify the reliability of the mesh strategy and calculation settings of this study, the numerical results from this article are compared with a CRH2 wind tunnel test (Zhang et al., 2018). Figure 10(a) and (b) show a 1/8 scale CRH2 high-speed train in the large-scale low-speed wind tunnel with dimensions of $16\,\text{m}\times8\,\text{m}\times6\,\text{m}$. The

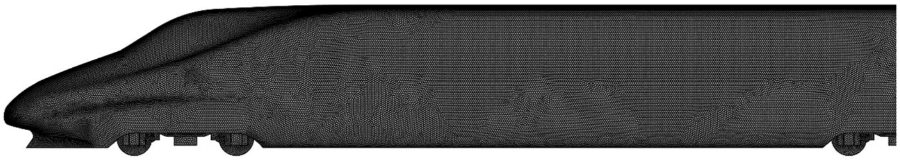

Figure 8. Surface meshes on the head car.

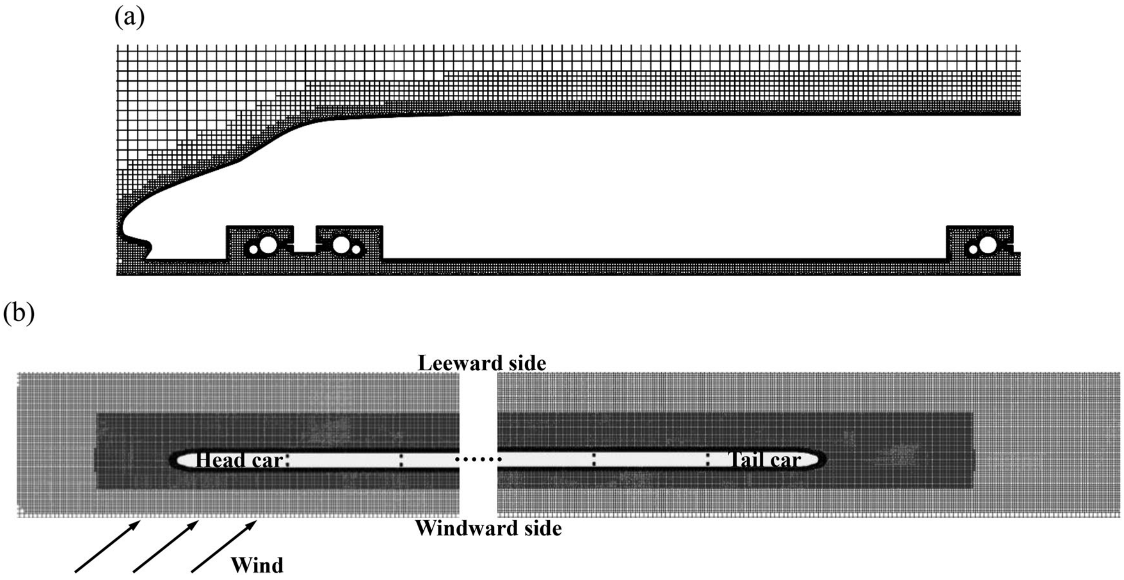

Figure 9. Volume meshes around the head car: (a) side view; and (b) top view.

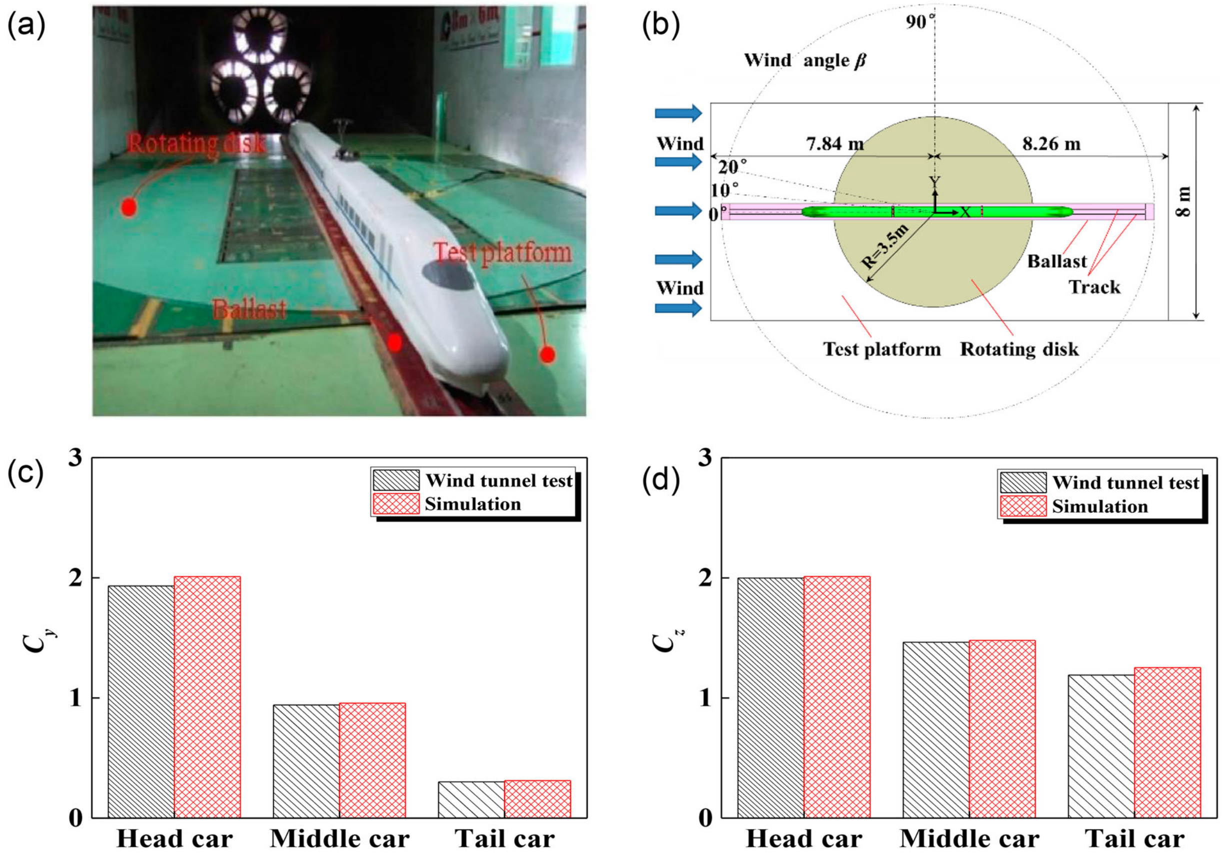

Figure 10. Results comparison between CFD simulation and wind tunnel test of CRH2 train: (a) train model in the wind tunnel; (b) location of the train model; (c) comparison of lateral force coefficient; and (d) comparison of lift force coefficient. The wind tunnel test data are obtained from Zhang et al., (2018).

ground of the wind tunnel was covered by a circular rotating slab with a diameter of 7 m to test the influence of different wind angles on the train aerodynamics. The train aerodynamics were monitored by a balance located inside its body. Figure 10(c) and (d) show a comparison between the numerical simulation results and the experiment results of different cars, regarding the lateral force coefficient C_y and lift force coefficient C_z. The wind speed is 60 m/s, and the yaw angle is 19.8°. Figure 10 shows the comparison of the lateral force coefficient C_y and lift force coefficient C_z between the numerical simulation of the head, middle, and tail cars and the experiment results. It should be noted that $C_y = \frac{F_y}{0.5\rho V^2 A}$, $C_z = \frac{F_z}{0.5\rho V^2 A}$, where F_y and F_z are respectively the lateral and lift forces, ρ is the air density of $1.225\,\mathrm{kg/m^3}$, V is the incoming flow speed of 60 m/s with a wind angle of 19.8°, and A is the train cross-sectional area of $11.23\,\mathrm{m^2}$. It can be found that the numerical simulation is very close to the experimental results, and the maximum error is less than 3%. It indicates that the calculation method and the grid strategy in this paper are reliable and can be used for subsequent analysis.

3.3. Computational results

Figure 11 compares the different vehicle aerodynamics under different train speeds. The aerodynamics of the first vehicle is significantly greater than the others, especially for the side force, rolling moment, pitch moment, and yaw moment. Except for the pitch moment, the aerodynamic signs of different vehicles are the same. In the pitch moment, the aerodynamic sign of the first vehicle is negative, while the aerodynamic signs of other vehicles are positive, which is related to the flow field around the first vehicle. In addition, with the growth of train velocity, the side force of the first vehicle increases obviously, while the rolling, pitch and yaw moments decrease clearly. In contrast, the lift exhibits only a slight change, which means that the train velocity mainly affects other aerodynamics rather than the lift force under crosswind. Overall, the aerodynamic variations among different vehicles of HSFT are similar to the findings of (Chen et al., 2018). Chen et al. (2018) found that in a strong wind environment, the aerodynamic drag coefficient was largest for the tail car, whereas the side force coefficient, lift coefficient, and roll moment coefficient were largest for the head car.

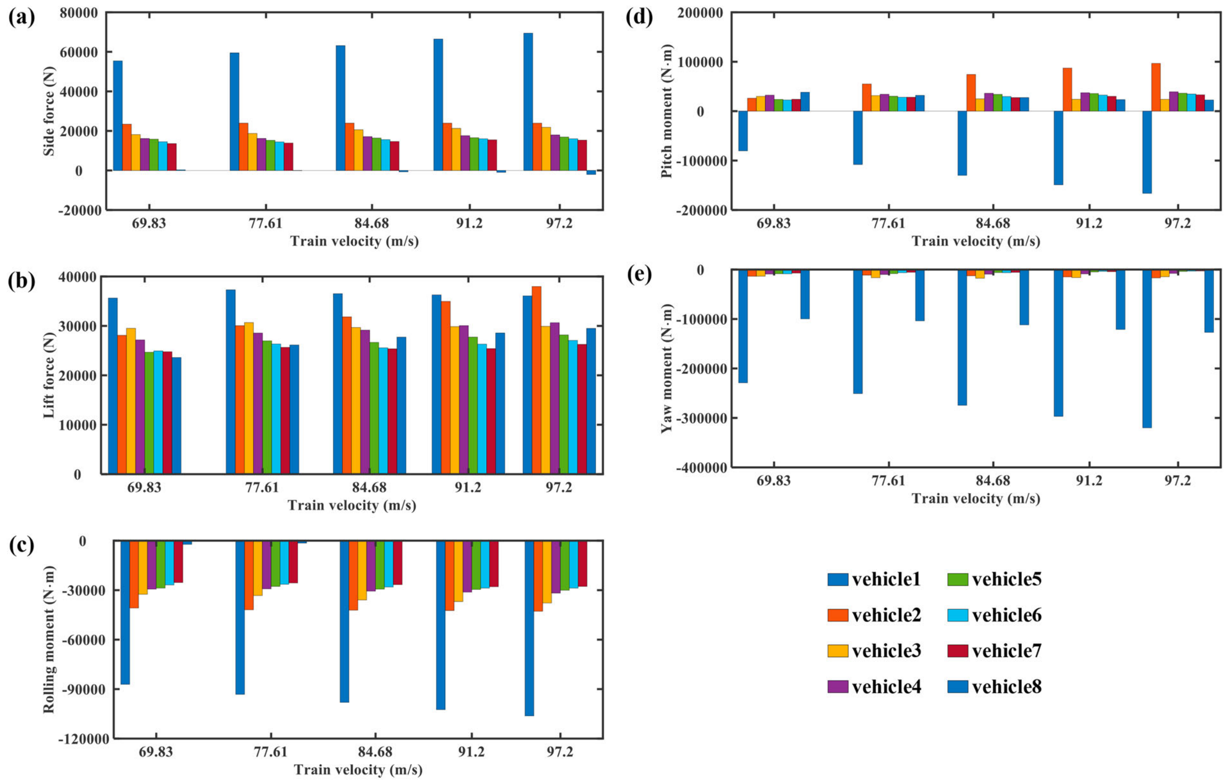

Figure 11. Vehicle aerodynamics under different train velocities: (a) side force; (b) lift force; (c) rolling moment; (d) pitch moment; and (e) yaw moment.

Figure 12 presents the velocity field at the half height of the train. It should be noted that the velocity is used as the variable of the contour. As the train velocity V_{tr} rises, the magnitude of the velocity fields around the train becomes larger and larger, which is related to the change in the relative velocity V_{α}. Moreover, the distributions of the velocity fields are obviously different under different train velocities, especially the separation region at the leeward of the train. The size of the separation region experiences a reduction during the increase of the train velocity V_{tr}, which corresponds to the variation of the relative wind angle β.

Since the aerodynamics of the first vehicle under the crosswind is the largest among all the vehicles, all the following analyses are based on the first vehicle. As shown in Figure 13, the windward and leeward pressure distributions of the first vehicle under different train velocities are compared. As the velocity of the train rises, the high-pressure regions on the windward vehicle head expand. For the leeward side, the low-pressure regions expand in head region with the rising train velocity. Those phenomena are related to the relative wind angle. As shown in Figure 12, with the enhancement of train velocity, the relative wind angle decreases to result in concentration of

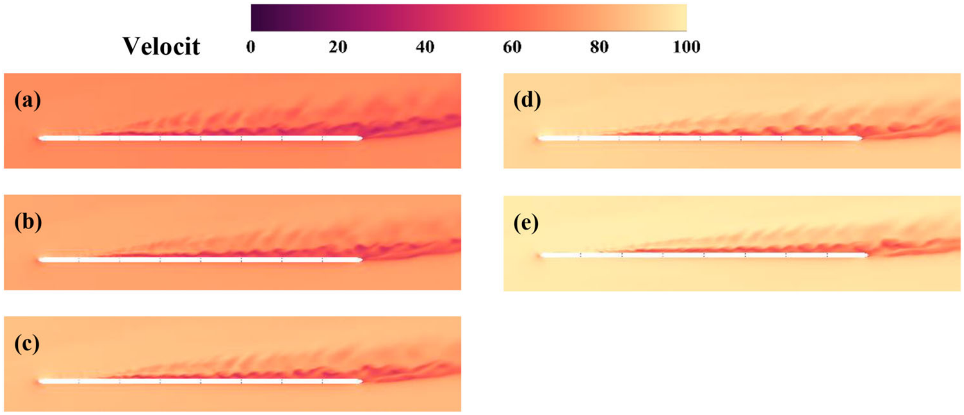

Figure 12. Velocity contour on the plane at the half height of the train for different train velocities V_{tr}: (a) 69.83; (b) 77.61; (c) 84.68; (d) 91.20; and (e) 97.20 m/s.

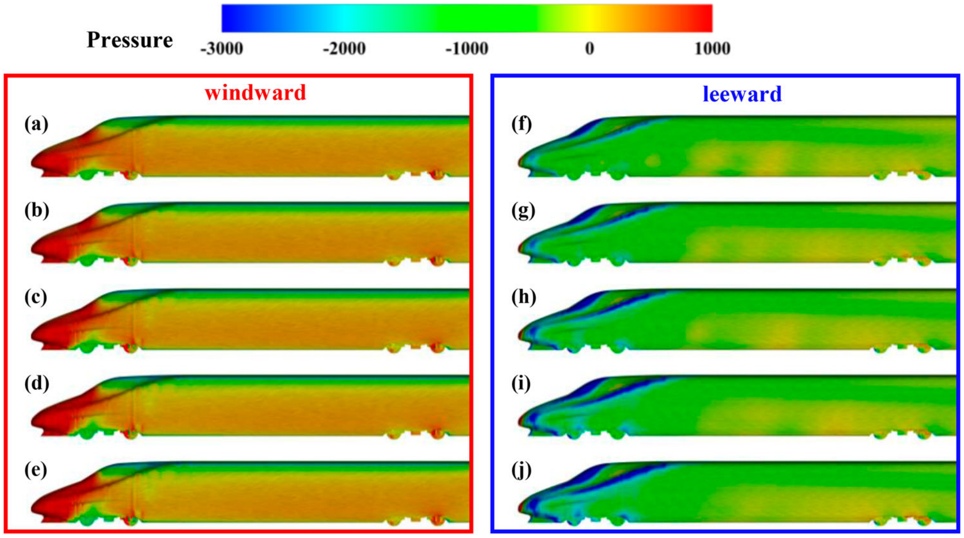

Figure 13. Pressure contour on the first vehicle for different train velocities V_{tr}: (a) and (f) at 69.83; (b) and (g) at 77.61; (c) and (h) at 84.68; (d) and (j) at 91.20; and (e) and (j) at 97.2 m/s. The windward side of the vehicle at the left column, and the leeward of the vehicle at the right column, pressure unit is Pa.

the direct crosswind action on the head of the first vehicle. It also corresponds to the aerodynamic variation in Figure 11. For instance, the absolute values of the side force and rolling moment increase with the expansions of the high-pressure regions on the windward side and the low-pressure regions on the leeward side. Moreover, the expansions of the high-pressure area and the low-pressure area at the head of the first vehicle lead to the gradual rise of the absolute values of the pitching moment and yaw moment.

To further verify the pressure distribution on the first vehicle, the pressure distributions on the plane x1 (at the head of the vehicle) and x2 (at the middle of the vehicle) are depicted in Figures 14 and 15, respectively. Among them, plane x1 is situated 4.44 m away from the nose of the train, while plane x2 is located 13.19 m away. As shown in Figure 14, the high-pressure regions on the windward change slightly. Meanwhile, the low-pressure regions on the head increase progressively. In Figure 15, it can be found out that although the pressure fields around the train do not differ a lot with different train velocities, the separation vortices at the leeward side become smaller and close to the train gradually.

4. Multibody dynamics simulation of the crosswind-vehicle model

The multibody dynamics simulation software VI-Rail is used to establish the crosswind-vehicle model. Based on the calculation results in Section 3, the first car in HSFT is adopted as the research objective because it is accompanied by the largest aerodynamic load.

4.1. Establishment of the crosswind-vehicle model

The crosswind-vehicle model of HSFT is made up of the CRH2C vehicle, cargo shipped by the vehicle, and the applied aerodynamic load.

4.1.1. Dynamics simulation model of CRH2C vehicle fixed with cargo

The vehicle model contains a car-body, two bogie frames, four wheelsets, and eight alxeboxes. All these parts are regarded as rigid bodies, which are connected by joints or constraints. The axle box is linked with the wheel by a revolute joint. The primary suspension, which contains a helical spring and a vertical damper, connects the axle box to the bogie frame. The second suspension, which contains three-dimensional springs and dampers, connects the bogie frame with the carbody. The main parameters of the vehicle model have already been introduced in (Zhai et al., 2015). The cargo is represented by a symmetrical cube, fixed with the carbody. In order to verify the accuracy of the established vehicle model, the mass of cargo is set as 22 t to meet the experimental conditions described in (Zhai et al., 2015). The German high-speed track irregularity is adopted as the track excitation in this work. The simulation result of the vertical carbody acceleration is compared with the in-situ test result in Figure 16. It can be seen that the simulation and test results show a good similarity, and the maximum error is small. Thus, the established vehicle model meets the requirements of this work.

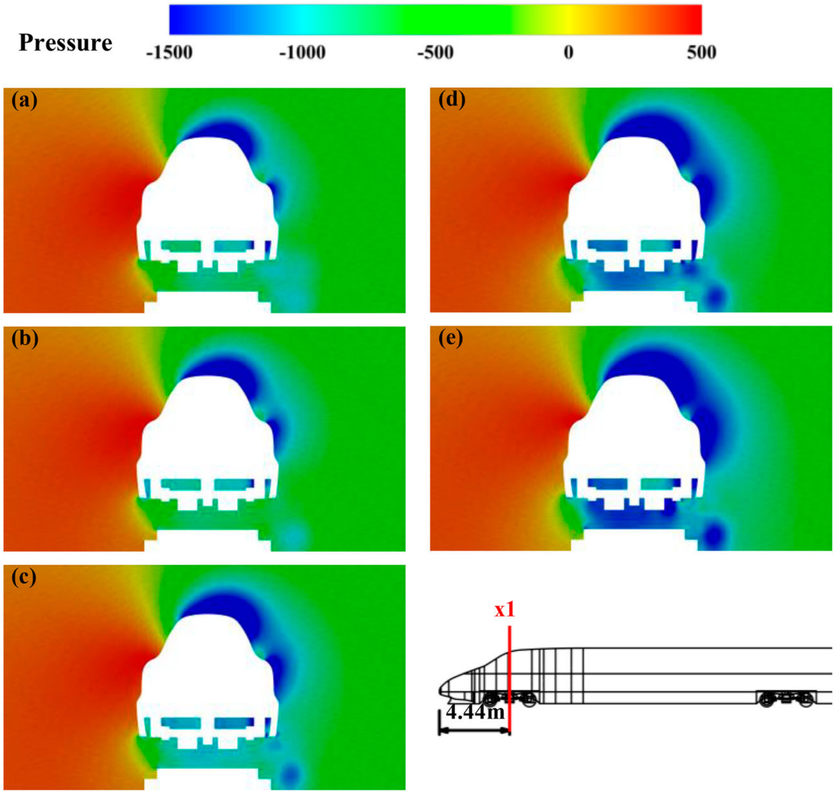

Figure 14. Pressure contour on the plane x1 for different train velocities V_{tr}: (a) 69.83; (b) 77.61; (c) 84.68; (d) 91.20; and (e) 97.20 m/s.

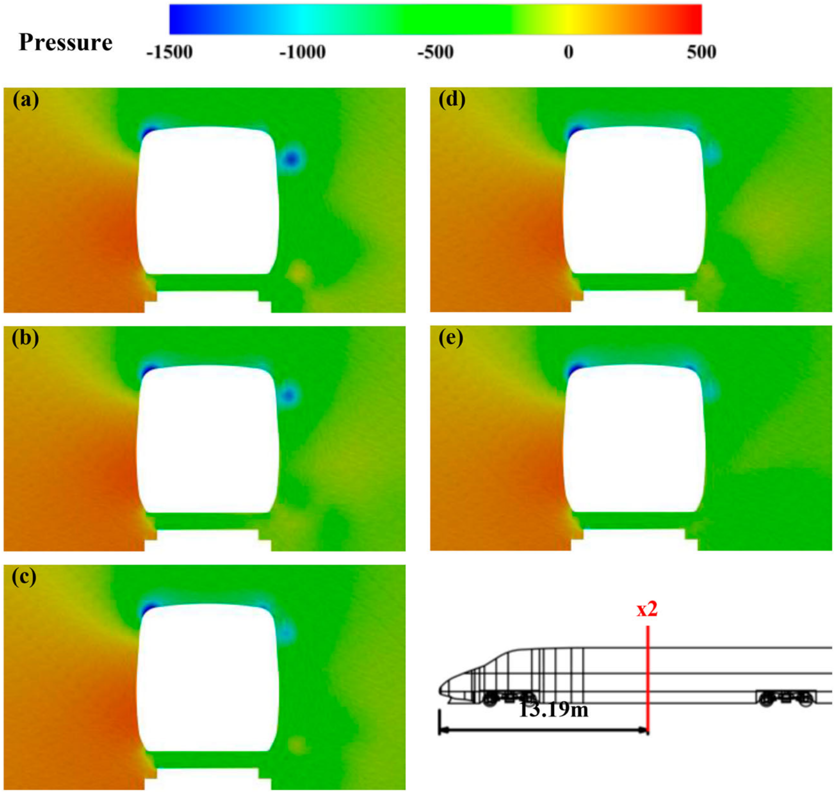

Figure 15. Pressure contour on the plane x2 for different train velocities V_{tr}: (a) 69.83; (b) 77.61; (c) 84.68; (d) 91.20; and (e) 97.20 m/s.

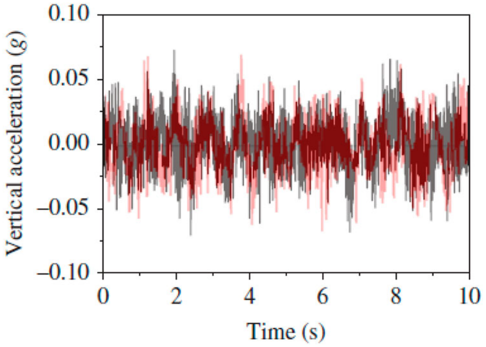

Figure 16. Comparison between the test and simulation results (Zhai et al., 2015), where the black line represents the test result and the red line represents the simulation result.

4.1.2. The action of aerodynamic load

The side wind force and lift wind force act at the geometry center of the vehicle model. The rolling, pitch and yaw moments induced by the crosswind act at the point located on the rail top in the centerline of the track. The aerodynamic load enhances to a stable level from 2 s to 12 s for each wind force and moment, as illustrated in Figure 17.

The imposed wind loads are the average values of the aerodynamic load for the first vehicle based on the calculation results in Section 3, as listed in Table 2.

The sign of the aerodynamic load denotes its direction in the coordinate system of the wind, as is shown in Figure 18.

In this Section, the vehicle model goes through a right-curve track. The left rail is higher than the right rail on curve for better curve negotiation performance. When the wind blows from the right side, we assume that the peak values are as large as the values listed in Table 2. Only the signs of F_T, M_{xx}, and M_{zz} should be revised according to the direction of wind.

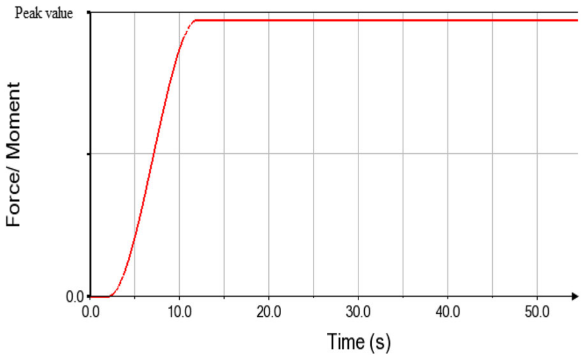

Figure 17. The action process of crosswind.

Table 2. Aerodynamic load for the vehicle model.

v(m/s)	F_T(N)	F_L(N)	M_{xx}(N·m)	M_{yy}(N·m)	M_{zz}(N·m)
69.83	55406.06	35630.67	−87094.90	−80346.13	−229004.44
77.61	59469.87	37298.96	−93206.56	−108024.89	−250889.89
84.68	63155.31	36519.31	−98027.63	−129869.43	−274503.61
91.20	66471.62	36268.39	−102441.25	−149152.54	−296820.78
97.20	69466.39	36084.58	−106219.54	−166283.33	−320075.21

4.2. Simulation results for transporting light weight cargo

4.2.1. Design of simulation cases

In this study, the cargo is regarded as a symmetrical cube because of the transport object of HSFT. It can be seen from Equations (16) and (17) that the density and height of the shipped cargo play a critical role in the overturning safety by determining the mass and gravity center height of the vehicle. In order to take full advantage of the transport capacity, we assume that the light weight cargo with low density can fill the inner space of HSFT sufficiently when its mass reaches the requirement of maximum axle load. The geometry characteristics of the assumed inner space based on the size of CRH2C car are illustrated in Figure 19.

Because the maximum axle load is 15 t, the maximum allowed cargo mass is 26 t. Hence, the minimum density of cargo is 250 kg/m^3 to realize full load, which is adopted as the density of light weight cargo in the simulation. Considering the value of H’, the selected values of H for the light weight cargo are designed as 0.26, 0.52, 0.78, 1.04, 1.30, 1.56, 1.82, 2.08, 2.34, and 2.60 m.

The crosswind-vehicle model will go through a track which has the length of 7560 m and contains straight line, transition curve line, and 3000-meter right curve line, as illustrated in Figure 20. Five vehicle velocities will be considered and the aerodynamic load varies as Table 2 shows.

4.2.2. Dynamic response of HSFT with light weight cargo

As an example, when the wind blows from the left side, the overturning coefficient of the fully loaded HSFT model with the speed of 69.83 m/s is illustrated in Figure 21.

Combined with the track layout shown in Figure 20 and the vehicle velocity, the trend in Figure 21 demonstrates that the train overturning safety has a close relationship with wind force and track conditions. From 2 s to 12 s, the safety index significantly increases with the enhancement of aerodynamic load. Then the fluctuation converges gradually on straight track from 12 s to 34 s. When the vehicle runs into the curve track through the transition curve from 34 s to 44 s, the overturning coefficient rises by degrees. After negotiating the curve track, the safety index keeps in a low level on the straight track after 97 s. In this study, we focus on the dynamic response

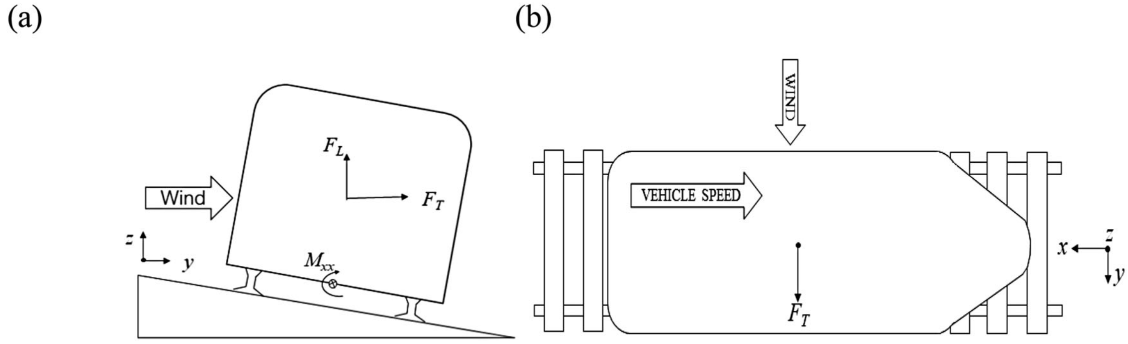

Figure 18. The direction of aerodynamic load: (a) front view; and (b) top view.

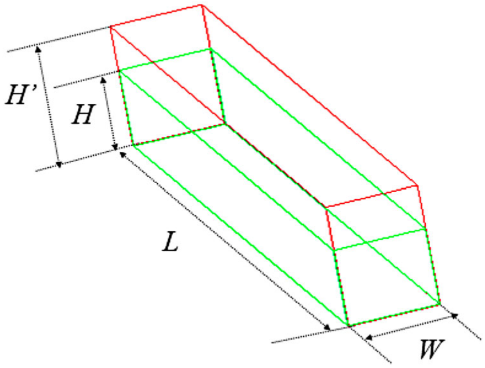

Figure 19. Schematic of the inner space of the vehicle for HSFT, where $L = 20$ m, $W = 2$ m, $H' = 2.6$ m, H denotes the height of the loaded cargo, the red cube denotes the inner space of the vehicle for HSFT.

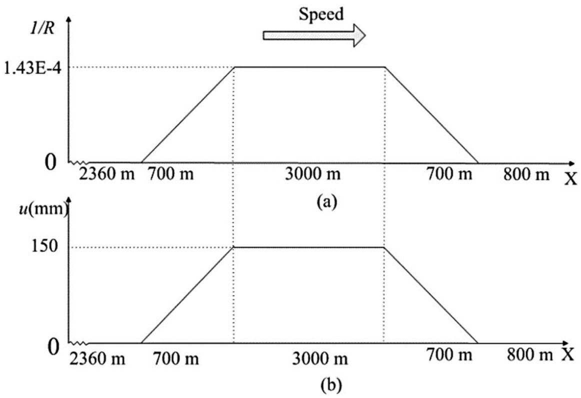

Figure 20. The layout of the test track, where R represents the curve radius, u represents the value of cant, and X represents the running direction of vehicle.

of HSFT in a steady strong wind field. Hence, the data on the curve track is collected for analysis.

The relationship among the overturning coefficient, cargo height, and vehicle velocity can be shown in Figure 22.

It is demonstrated that enhancing the cargo quantity is good for overturning safety, no matter the wind blows from which side. It should be noted that the correlation between cargo quantity and overturning coefficient is not as strong as the correlations between the overturning coefficient and the height of vehicle gravity center (Thomas et al., 2010) or vehicle mass (Heleno et al., 2021). This special phenomenon occurs because the increase of cargo quantity will generate larger cargo mass, as well as higher vehicle gravity center. These two factors have opposite effects on the overturning coefficient.

As is shown in Figure 22, *D* basically rises with the improvement of vehicle velocity because of the enhancements of centrifugal force and aerodynamic load. When the wind blows from the left side, which is the outer side of the curve track, the lateral aerodynamic load can weaken the effect of unbalanced centrifugal force at a high level of speed. Thus, the overturning safety of HSFT under high velocity can be significantly improved with the growth of cargo quantity, as illustrated in Figure 22(a). According to the Chinese standard (GB-5599-85) (China Standard Bureau, 1986), the overturning coefficient should be smaller than 0.8 for the sake of vehicle running safety. Based on the data shown in Figure 22, HSFT speed should be decreased according to the shipped cargo mass. For a fully loaded HSFT, the maximum vehicle speed can be up to 305 km/h under the steady wind whose speed is 20 m/s. Niu et al. (2018) introduced that the operational speed of CRH2C high-speed train is 300 km/h when the average wind speed is 20 m/s. Because the established HSFT model in this paper is based on CRH2C high-speed train, the conclusions about the operational speed for HSFT basically agree with previous experience.

Based on the contrast as illustrated in Figure 23, it is obvious that the wind from right side is a greater threat to overturning safety for most cases. The worse influence of wind from left side occurs only when the HSFT runs safely with a heavy cargo mass and low speed. Thus, we can use the values of overturning coefficient under the strong wind from right side to evaluate the overturning safety of HSFT under the crosswind.

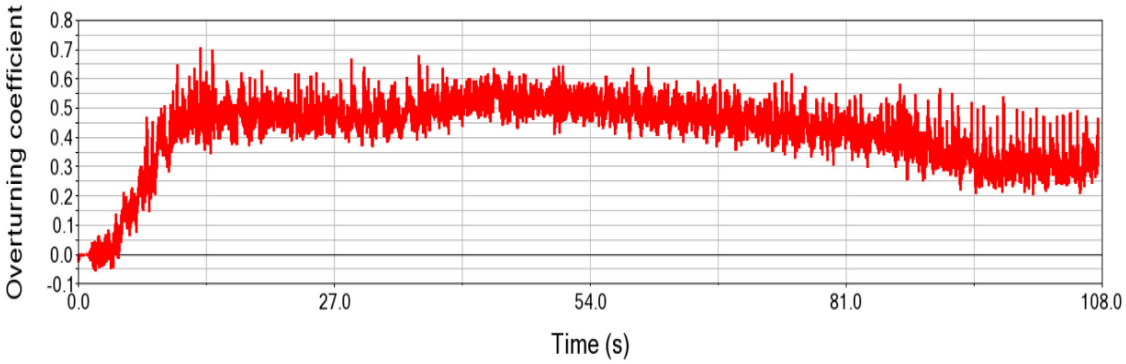

Figure 21. Times history of the overturning coefficient.

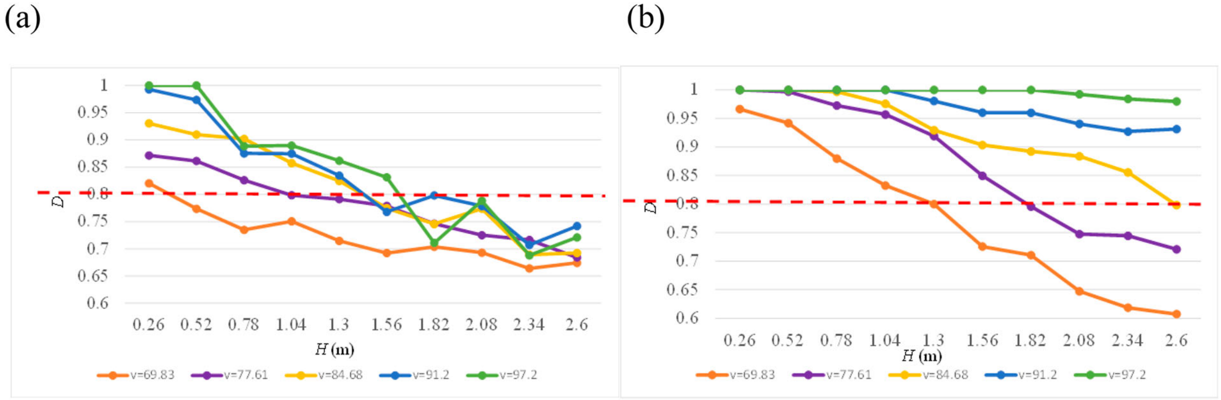

Figure 22. The peak overturning coefficient of HSFT in the strong wind field: (a) wind from left side; and (b) wind from right side.

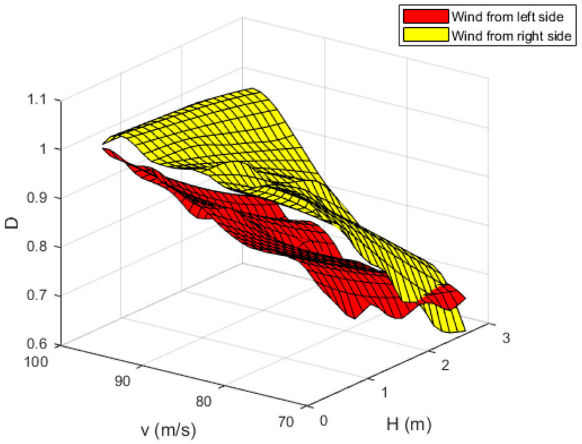

Figure 23. Dynamic responses with different wind directions.

The influence of wind direction on curve track is highlighted in Figure 24. It should be noted that the differences are very small when H is small and v is large because the train could overturn in this situation, no matter the wind blows from which side. Hence, this part of data should not be considered when the effect of wind direction is investigated. As analyzed in Section 2, the combined action of cant deficiency and aerodynamic results in different dynamic responses under different wind directions. With the growth of vehicle speed, the aerodynamic load enhances significantly. When the wind blows from inner side of the curve track and there is cant deficiency, the direction of side wind force is in accordance with unbalanced centrifugal force which is in proportion to cargo mass. Thus, the crosswind from inner side would aggravate the train overturning at high speed. Chen et al. (2009) likewise demonstrated that when the wind blows from the inner rail to the outer rail, the running speed of high-speed train should be reduced, compared with the situation when the wind blows from the outer rail to the inner rail. As revealed in Figure 24, the wind from inner side is good only for the HSFT with large cargo mass and low speed, because the side wind force can neutralize the unbalanced gravity in lateral direction in this situation.

4.3. Comparison results for different cargo densities

Figure 22 illustrates that the growth of cargo quantity plays an active role in vehicle overturning safety. Based on Equations (16) and (17), both the cargo mass and vehicle gravity center height will change along with the variations in cargo quantity and density. In **4.2**, the overturning safety of HSFT with light cargo has been evaluated. Then we double the density of cargo to 500 kg/m^3 and regard such cargo as the heavy cargo. The possible heights of heavy cargo are designed as 0.13, 0.26, 0.39, 0.52, 0.65, 0.78, 0.91, 1.04, 1.17, and 1.30 m. Thus, the heavy cargo has the same mass as the light cargo with the same rank of cargo height. Because the HSFT will overturn with the speed of 97.2 m/s, as shown in Figure 22(b), the dynamic response of the HSFT with heavy cargo is tested under 4 speed levels. Considering the larger effect on train overturning safety, the simulation results for the HSFT with the inner side wind are illustrated in Figure 25. Due to the same maximum shipped cargo mass, the proportion of cargo mass to the maximum value is used to describe the value of cargo mass. Obviously, the height for heavy cargo is half of that for light cargo with the same mass.

Same as Figure 24, some data in Figure 25(b) shouldn't be considered because the overturning coefficient equals 1.0. According to inherent cognition, the enhancement in cargo density has a positive role in overturning safety because the vehicle gravity center height can be decreased. Whereas Figure 25 proves that decreasing the cargo density, which means increasing the cargo gravity center height, can overcome the negative effect of inner side wind at a low vehicle speed. In this situation, the overturning moment induced by wind load is weakened by the moment which is induced by the unbalanced gravity and rises with the increase of cargo quantity. However, when the vehicle is not adequately loaded or the vehicle speed is large, it is necessary to improve the cargo density for the sake of train overturning safety. Hazrati Ashtiani et al. (2015) proposed that the higher cargo density would lead to better dynamics performance for a railway tank car, which is in agreement with the conclusions drawn in this paper.

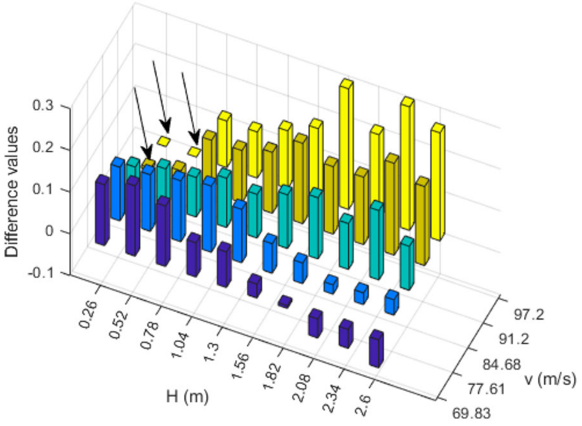

Figure 24. Difference of *D* values between the inner side wind and outer side wind.

5. Conclusions

In order to reveal the relationship between cargo properties and the overturning safety of HSFT under strong winds, the crosswind-vehicle vibration model is established and validated by the wind tunnel test and in-situ test. Based on the results of dynamics simulations with the maximum aerodynamic load, optimization strategies of cargo properties are proposed. The conclusions are drawn as follows:

(1) For an eight-car CRH2C train, the aerodynamics of the first vehicle is obviously the highest among all the vehicles. As the train velocity rises, the absolute values of the side force, rolling moment, pitch moment, and yaw moment increase obviously, while the lift force does not change significantly.
(2) The inner side crosswind is a greater threat to train overturning safety than the outer side crosswind. The direction of the resultant force for the lateral

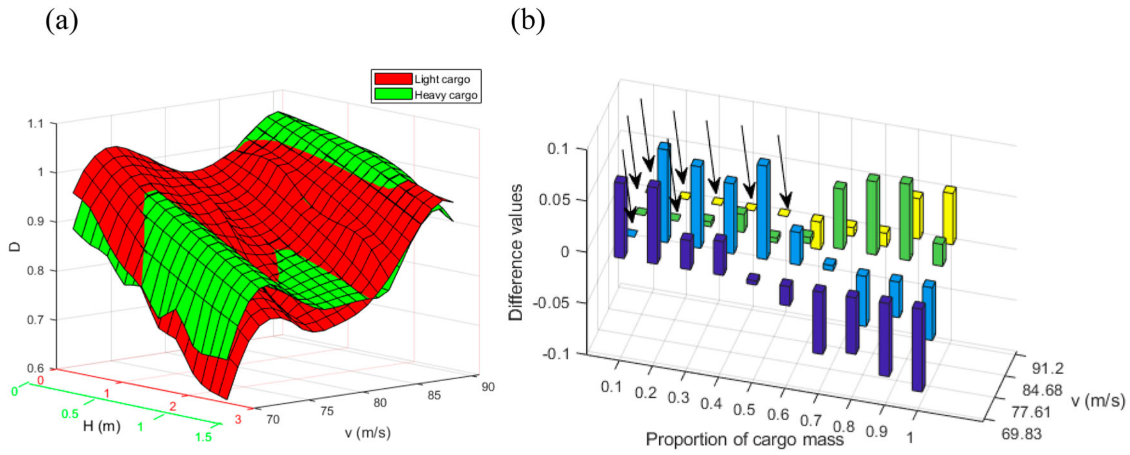

Figure 25. The contrast of HSFT with different cargoes under inner side wind: (a) peak values of overturning coefficient; and (b) difference between the vehicle with light cargo and the vehicle with heavy cargo.

components of gravity and centrifugal force depends on the vehicle velocity. The synergistic action of unbalanced centrifugal force and the side wind force from the inner side aggravates the risk of overturning under high velocity.

(3) The cargo quantity plays a positive role in train overturning safety. When the HSFT is fully loaded, the vehicle speed can be as large as 305 km/h under the condition of a 20 m/s steady crosswind. If the cargo quantity decreases, the HSFT should slow down accordingly.

(4) Enhancing the cargo density has a good effect on the train overturning safety with high vehicle speed or low load factor, which are severe working conditions under strong winds. Hence, it should be encouraged to transport high-density cargo by HSFT.

The quantitative conclusions drawn in this paper are conservative because the maximum aerodynamic load is imposed on the crosswind-vehicle model. The requirements of cargo properties for each vehicle of a high-speed freight train should be different with their respective aerodynamic loads. How to assign the cargo among all the vehicles in a high-speed freight train deserves further investigation.

Disclosure statement

No potential conflict of interest was reported by the author(s).

Funding

The work described in this paper was supported by the National Natural Science Foundation of China (Grant No. 52202426), the Open Project of Key Laboratory of Traffic Safety on Track of Ministry of Education, Central South University (Grant No. 502401002), Start-up Fund for RAPs under the Strategic Hiring Scheme of The Hong Kong Polytechnic University (Grant No. 1-BD23), the Natural Science Foundation of Hunan Province, China (Grant No. 2020JJ4737). The work described in this paper was also supported by a grant (RIF) from the Research Grants Council of the Hong Kong Special Administrative Region (SAR), China (Grant No. R-5020-18) and a grant from the National Natural Science Foundation of China (Grant No. U1934209). The authors would also like to appreciate the funding supported by the Innovation and Technology Commission of the Hong Kong SAR Government (Grant No. K-BBY1), the Hong Kong and Macau Joint Research and Development Fund of Wuyi University (Grants No. 2019WGALH15, 2019WGALH17, 2021WGALH15), Guangdong Basic and Applied Basic Research Fund for Guangdong-Hong Kong-Macao Research Team Project (Grant No. 2021B1515130006),. and The Hong Kong Polytechnic University's Postdoctoral Matching Fund Scheme [grant number 1-W21X].

References

Boehm, M., Arnz, M., & Winter, J. (2021). The potential of high-speed rail freight in Europe: How is a modal shift from road to rail possible for low-density high value cargo? *European Transport Research Review*, *13*(1), 1–11. https://doi.org/10.1186/s12544-020-00453-3

Chen, R., Zeng, Q., Zhong, X., Xiang, J., Guo, X., & Zhao, G. (2009). Numerical study on the restriction speed of train passing curved rail in cross wind. *Science in China Series E: Technological Sciences*, *52*(7), 2037–2047. https://doi.org/10.1007/s11431-009-0202-5

Chen, Z., Liu, T., Guo, Z., Huo, X., Li, W., & Xia, Y. (2022). Dynamic behaviors and mitigation measures of a train passing through windbreak transitions from ground to cutting. *Journal of Central South University*, *29*, 2675–2689. https://doi.org/10.1007/s11771-022-5114-6

Chen, Z., Liu, T., Jiang, Z., Guo, Z., & Zhang, J. (2018). Comparative analysis of the effect of different nose lengths on train aerodynamic performance under crosswind. *Journal of Fluids and Structures*, *78*, 69–85. https://doi.org/10.1016/j.jfluidstructs.2017.12.016

Chen, Z., Liu, T., Yu, M., Chen, G., Chen, M., & Guo, Z. (2020). Experimental and numerical research on wind characteristics affected by actual mountain ridges and windbreaks: A case study of the Lanzhou-Xinjiang high-speed railway. *Engineering Applications of Computational Fluid Mechanics*, *14*(1), 1385–1403. https://doi.org/10.1080/19942060.2020.1831963

China Standard Bureau. (1986). GB5599-85.Railway vehicles-specification for evaluation the dynamic performance and accreditation test.

China Youth International. (2020). The world first! 350 kilometers per hour! The domestic high-speed freight EMU is here.

Deng, E., Yang, W., Deng, L., Zhu, Z., He, X., & Wang, A. (2020). Time-resolved aerodynamic loads on high-speed trains during running on a tunnel-bridge-tunnel infrastructure under crosswind. *Engineering Applications of Computational Fluid Mechanics*, *14*, 202–221. https://doi.org/10.1080/19942060.2019.1705396

Deng, G., Peng, Y., Yan, C., & Wen, B. (2021). Running safety evaluation of a 350 km/h high-speed freight train negotiating a curve based on the arbitrary Lagrangian-Eulerian method. *Proceedings of the Institution of Mechanical Engineers, Part F: Journal of Rail and Rapid Transit*, *235*(9), 1143–1157. https://doi.org/10.1177/0954409720986283

EN 14067-6. (2010). *Railway applications-aerodynamics part 6: Requirements and test procedures for cross wind assessment*. British Standard Institute.

German Aerospace Center. (2018). *Researching the next generation train*.

Hazrati Ashtiani, I., Rakheja, S., Ahmed, A. K. W., & Zhang, J. (2015, March). Hunting analysis of a partially-filled railway tank car. In *ASME/IEEE joint rail conference* (Vol. 56451, p. V001T10A003). American Society of Mechanical Engineers.

Heleno, R., Montenegro, P. A., Carvalho, H., Ribeiro, D., Calcada, R., & Baker, C. J. (2021). Influence of the railway vehicle properties in the running safety against crosswinds. *Journal of Wind Engineering And Industrial Aerodynamics*, *217*, 104732. https://doi.org/10.1016/j.jweia.2021.104732

Hibino, Y., Shimomura, T., & Tanifuji, K. (2010). Full-scale experiment on the behavior of a railway vehicle being subjected to lateral force. *Journal of Mechanical Systems for Transportation and Logistics*, *3*, 35–43. https://doi.org/10.1299/jmtl.3.35

Iwnicki, S., Bezin, Y., Orlova, A., Johnsson, P., Stichel, S., & Schelle, H. (2013). The 'SUSTRAIL' high speed freight vehicle: Simulation of novel running gear design. *System*, *5*, 20.

Liu, D., Tomasini, G. M., Cheli, F., Zhong, M., Zhang, L., & Lu, Z. (2022). Effect of aerodynamic force change caused by car-body rolling on train overturning safety under strong wind conditions. *Vehicle System Dynamics*, *60*, 433–453. https://doi.org/10.1080/00423114.2020.1817508

Liu, D., Tomasini, G. M., Rocchi, D., Cheli, F., Lu, Z., & Zhong, M. (2020). Correlation of car-body vibration and train overturning under strong wind conditions. *Mechanical Systems And Signal Processing*, *142*, 106743. https://doi.org/10.1016/j.ymssp.2020.106743

Liu, T., Chen, Z., Zhou, X., & Zhang, J. (2018). A CFD analysis of the aerodynamics of a high-speed train passing through a windbreak transition under crosswind. *Engineering Applications of Computational Fluid Mechanics*, *12*(1), 137–151. https://doi.org/10.1080/19942060.2017.1360211

Maleki, S., Thompson, B. D., & C, M. (2020). On the flow past and forces on double-stacked wagons within a freight train under cross-wind. *Journal of Wind Engineering And Industrial Aerodynamics*, *206*, 104224. https://doi.org/10.1016/j.jweia.2020.104224

National Railway Administration of People's Republic of China. (2014). *Code for design of high speed railway*. China Railway Publishing House Co., Ltd.

Niu, J. Q., Zhou, D., & Liang, X. F. (2018). Numerical simulation of the effects of obstacle deflectors on the aerodynamic performance of stationary high-speed trains at two yaw angles. *Proceedings of the Institution of Mechanical Engineers, Part F: Journal of Rail and Rapid Transit*, *232*(3), 913–927. https://doi.org/10.1177/0954409717701786

Optoelectronics Science And Technology. (2020). China's high-speed freight EMU is offline, with a speed of 350 kilometers per hour. More than disassembling the seat.

Schubert, M., Kluth, T., Nebauer, G., Ratzenberger, R., Kotzagiorgis, S., Butz, B., Schneider, W., & Leible, M. (2014). *Verkehrsverflechtungsprognose 2030. Zusammenfassung der Ergebnisse*. BVU/ITP/IVV/Planco.

Soper, D. (2016). *The aerodynamics of a container freight train*. Springer.

Thomas, D., Diedrichs, B., Berg, M., & Stichel, S. (2010). Dynamics of a high-speed rail vehicle negotiating curves at unsteady crosswind. *Proceedings of the Institution of Mechanical Engineers, Part F: Journal of Rail and Rapid Transit*, *224*, 567–579. https://doi.org/10.1243/09544097JRRT335

Wang, F. (Ed.). (1994). *Vehicle System Dynamics*. China Railway Publishing House.

Watson, I., Ali, A., & Bayyati, A. (2018). An investigation into the benefits and constraints of shifting freight traffic onto high-speed railways. *COMPRAIL 2018, Wessex Institute of Technology (WIT)*.

Watson, I., Ali, A., & Bayyati, A. (2019). Freight transport using high-speed railways. *International Journal of Transport Development and Integration*, *3*(2), 103–116. https://doi.org/10.2495/TDI-V3-N2-103-116

Xue, R., Ren, Z., Fan, T., & Rakheja, S. (2022). Vertical vibration analysis of a coupled vehicle-container model of a high-speed freight EMU. *Vehicle System Dynamics*, *60*(4), 1228–1252. https://doi.org/10.1080/00423114.2020.1850810

Yang, N., Feng, F., Huang, Q., & Liu, X. (2021). Optimized design to adverse transportation conditions for railway freight system. *Accident Analysis & Prevention*, *154*, 106091. https://doi.org/10.1016/j.aap.2021.106091

Zhai, W., Liu, P., Lin, J., & Wang, K. (2015). Experimental investigation on vibration behaviour of a CRH train at speed of 350 km/h. *International Journal of Rail Transportation*, *3*(1), 1–16. https://doi.org/10.1080/23248378.2014.992819

Zhang, D., Tang, Y., & Peng, Q. (2023). A novel approach for decreasing driving energy consumption during coasting and cruise for the railway vehicle. *Energy*, *263*, 125615. https://doi.org/10.1016/j.energy.2022.125615

Zhang, D., Tang, Y., Peng, Q., Dong, C., & Ye, Y. (2021). Effect of mass distribution on curving performance for a loaded wagon. *Nonlinear Dynamics*, *104*, 2259–2273. https://doi.org/10.1007/s11071-021-06386-3

Zhang, D., Tang, Y., Sun, Z., & Peng, Q. (2022). Optimising the location of wagon gravity centre to improve the curving performance. *Vehicle System Dynamics*, *60*(5), 1627–1641. https://doi.org/10.1080/00423114.2020.1865546

Zhang, L., Yang, M., & Liang, X. (2018). Experimental study on the effect of wind angles on pressure distribution of train streamlined zone and train aerodynamic forces. *Journal of Wind Engineering And Industrial Aerodynamics*, *174*, 330–343. https://doi.org/10.1016/j.jweia.2018.01.024